Interference features in scanning gate conductance maps of quantum point contacts with disorder

K. Kolasiński and B. Szafran
AGH University of Science and Technology, Faculty of Physics and Applied Computer Science, aleja Mickiewicza 30, 30-059 Kraków, Poland

B. Brun and H. Sellier
Université Grenoble Alpes, F-38000 Grenoble, France and CNRS, Institut NEEL, F-38042 Grenoble, France

(Received 24 March 2016; revised manuscript received 3 June 2016; published 3 August 2016)

We consider quantum point contact (QPC) defined within a disordered two-dimensional electron gas as studied by scanning gate microscopy. We evaluate the conductance maps in the Landauer approach with a wave-function picture of electron transport for samples with both low and high electron mobility at finite temperatures. We discuss the spatial distribution of the impurities in the context of the branched electron flow. We reproduce the surprising temperature stability of the experimental interference fringes far from the QPC. Next, we discuss funnel-shaped features that accompany splitting of the branches visible in previous experiments. Finally, we study elliptical interference fringes formed by an interplay of scattering by the pointlike impurities and by the scanning probe. We discuss the details of the elliptical features as functions of the tip voltage and the temperature, showing that the first interference fringe is very robust against the thermal widening of the Fermi level. We present a simple analytical model that allows for extraction of the impurity positions and the electron-gas depletion radius induced by the negatively charged tip of the atomic force microscope, and apply this model on experimental scanning gate images showing such elliptical fringes.

DOI: 10.1103/PhysRevB.94.075301

I. INTRODUCTION

Scanning gate microscopy (SGM) is an experimental technique which probes the transport properties of systems based on a two-dimensional electron gas (2DEG) using the charged probe of an atomic force microscope (AFM) [1–3]. A negatively charged AFM tip induces a finite-size depletion in the 2DEG, which acts as a movable scatterer of size and location controlled by the voltage applied to the SGM tip and its position above the sample [4]. The SGM technique was used first to investigate the electron transport in quantum point contacts (QPCs) [5]. The SGM conductance maps recorded as a function of the tip position in the vicinity of a QPC contain two characteristic features: (i) interference fringes with oscillation period equal to half the Fermi wavelength λ_F [6–12] and (ii) semiclassical branched flow of electron trajectories [9,13–15]. The fringes (i) arise from the coherent interference between the electron waves incident from the QPC and backscattered by the SGM tip [9,16]. The branched flow (ii) stems from the smooth potential disorder in the high-mobility semiconductor structures [9]. For low-mobility samples, the hard-impurity scattering is dominant and leads to coherent fringes which are surprisingly thermally stable, with the interference pattern visible at a distance from the QPC which largely exceeds the thermal length λ_{th} [6,7,9]. This surprising behavior is explained [6,7,9] by coherent scattering involving the tip and nearby impurities spaced by a distance below λ_{th}.

In this paper, we consider numerical simulations of a coherent branched flow of electrons spreading from a QPC. We study the effect of smooth and hard impurities on the transport for both low and high density of scatterers, i.e., for high- and low-mobility samples, respectively. For low-mobility samples, most of the features visible in the experimental SGM images can be explained in terms of a one-dimensional (1D) model of the branch, including (i) thermally persistent fringes visible at $T \simeq 4$ K, (ii) reappearance of fringes in some part of SGM images far from the QPC, and (iii) frequency of the fringes near the impurities that changes with T. We discuss splittings of the branches at some defects and funnel-shaped features that accompany the splitting.

We also consider high-mobility samples and indicate, by both experiment and theory, distinct signatures of a few hard scatterers present within the system that produce pronounced elliptical features in the SGM conductance maps. These elliptical features result from interference involving both the scatterer and the tip and remain stable up to at least $T \simeq 4$ K. We provide a simple model to describe these nearly elliptical contours which allows one to indicate the position of the scatterer within the sample, and the size of the area depleted by the tip.

II. MODEL

We consider a 2DEG system with a local constriction formed by the QPC (Fig. 1). The electrons are fed from the input lead at the left of the QPC. Behind the QPC, the electrons propagate freely, with open boundary conditions denoted by arrows at the blue edge of Fig. 1(a). We consider the scattering of the Fermi-level electrons solving the effective-mass Schrödinger equation (atomic units are used)

$$-\frac{1}{2m_{\text{eff}}}\nabla^2\Psi + V_{\text{tot}}\Psi = E_F\Psi, \tag{1}$$

where $\Psi \equiv \Psi(x,y)$ is the two-dimensional scattering wave function with density $\rho = |\Psi|^2$, and $m_{\text{eff}} = 0.067$ is the GaAs electron effective mass. In Eq. (1), $V_{\text{tot}} = V_{\text{QPC}} + V_{\text{tip}} + V_{\text{dis}}$ contains contributions of all possible sources of electrostatic potentials considered in this paper. We assume $E_F = 15$ meV, which corresponds to 2DEG density of 4.2×10^{11} cm^2. V_{QPC}

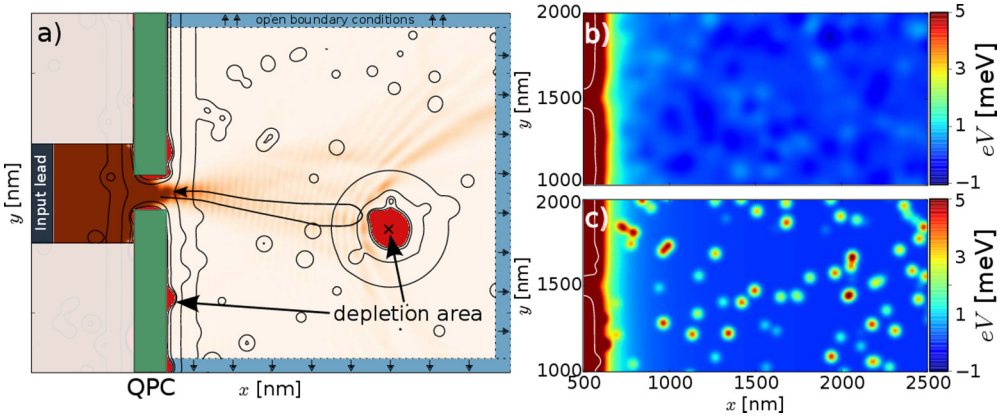

FIG. 1. (a) The sketch of the system. The loop marked by the black arrow schematically shows the scattering process leading to the $\lambda_F/2$ fringes in SGM images. The brown map shows the calculated scattering electron density plotted as $\sqrt{\rho}$. Disordered potential landscape in the sample near QPC for the case of (b) *smooth* impurities and (c) *hard* impurities. White solid lines in (b) and (c) show the isolines of the potential energy for $eV_{\rm tot} = E_F$. The QPC is tuned to the first plateau.

is the QPC electrostatic potential modeled with the Davies formula [17] for a finite rectangular gate [green rectangles on Fig. 1(a)],

$$V_{\rm QPC}/V_g = g(x-L,y-B) + g(x-L,T-y) + g(R-x,y-B) + g(R-x,T-y),$$

where $g(u,v) = \frac{1}{2\pi}\arctan\left(\frac{uv}{dP}\right)$; $P = \sqrt{v^2+u^2+d^2}$, with L, R, B, and T being the left, right, bottom, and top position of the gate edges [see Fig. 1(a)]. We choose the distance between 2DEG and gates to be $d = 50$ nm. In the above formula, V_g is the gate potential. For the applied parameters, the Fermi energy $E_F = 15$ meV corresponds to the first conductance plateau of the QPC. $V_{\rm tip}$ is the electrostatic potential of the charged tip, for which we use the Lorentzian approximation,

$$V_{\rm tip} = \frac{d_{\rm tip}^2 V_t}{(x-x_{\rm tip})^2 + (y-y_{\rm tip})^2 + d_{\rm tip}^2}. \quad (2)$$

The Lorentzian form of the tip potential arises due to screening by the electron gas inside the heterostructure [18–20]. The width of the tip is of the order of the tip-2DEG distance and fixed at $d_{\rm tip} = 80$ nm. The maximum potential change V_t induced by the tip in the 2DEG is taken to be 30 meV (except otherwise stated), corresponding to a depletion area of radius $d_{\rm tip}$. This simple form of tip potential corresponds to the case of linear screening by the 2DEG electrons [18,19], while the more complicated case with 2DEG depletion (i.e., when $V_t > E_F$) would require self-consistent numerical calculations. Finally, the last contribution to the potential, $V_{\rm dis}$, arises from the disorder in the donor layer and it is assumed to be a superposition of uniformly distributed Gaussian functions,

$$V_{\rm dis}(x,y) = \sum_{i=1}^{N_{\rm dis}} \alpha_i e^{-|r-r_i|^2/2\sigma^2},$$

where $N_{\rm dis}$ is the number of impurities, α_i is the potential amplitude of the ith impurity, r_i is the center of the ith Gaussian, and the same σ is applied for all Gaussians. The random positions of r_i are generated with a uniform distribution. The values of α_i are generated also with a uniform distribution within the range $|\alpha_i| < V_{\rm max}$. In the paper, we distinguish between hard and soft impurities. For the *hard* impurities, we take $V_{\rm max} = 0.3 \times E_F$, $\alpha_i > 0$, and $\sigma = 12$ nm, while for the *soft* impurities, $\sigma = 30$ nm and $V_{\rm max} = 0.05 \times E_F$ are applied.

We use the finite-difference discretization of Eq. (1) and wave-function matching (WFM)—described in the Appendices—in order to include the effect of the leads into the Hamiltonian and calculate the scattering amplitudes [21–23]. The conductance of the system is then calculated from the

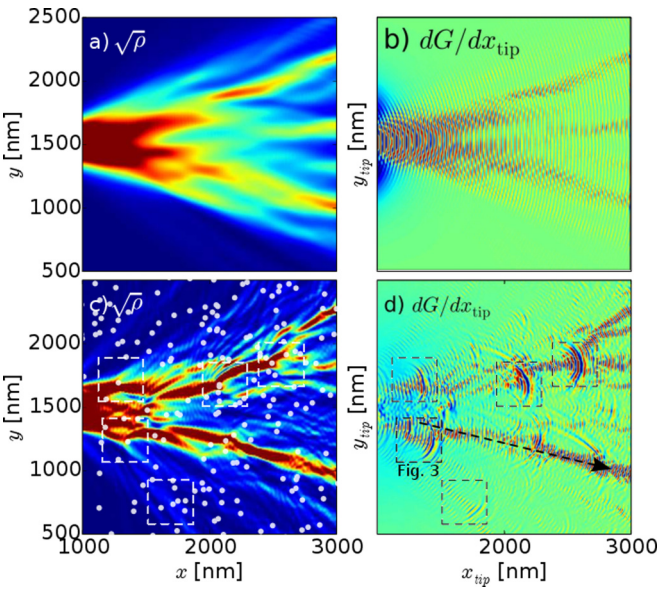

FIG. 2. (a) Square root of scattering electron density $\sqrt{\rho}$ for the case of smooth impurity background potential. (b) Simulated dG/dx SGM image. (c),(d) Same as (a) and (b), but for hard impurities. Squares in (c) and (d) denote the funnel-like fringe pattern discussed in the text. In (c) and (d), we considered $N_d = 500$ impurities within the entire computational box. In (a) and (b), we kept all of the impurities of (c) and (d) and inserted another 500 placed at random positions.

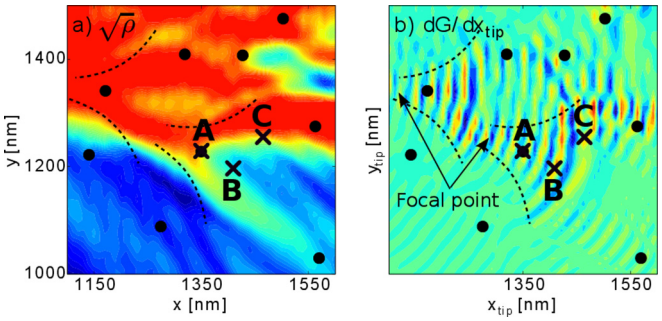

FIG. 3. Zoom of area denoted by "Fig. 3" square in Fig. 2(d). Points A, B, and C denote the possible tip positions of the scattering scenario schematically presented in Figs. 4(b), 4(c), and 4(d), respectively. Black dots represent the centers of the hard scatterers from Fig. 2(d). Panel (a) shows the square roof of the scattering density, and (b) the derivative of the conductance with respect to the tip position.

Landauer formula,

$$G(E_F,T) = G_0 \int_{-\infty}^{+\infty} dE\, M(E) \left[-\frac{\partial f(E;E_F,T)}{\partial E} \right], \qquad (3)$$

where $f(E;E_F,T) = 1/\{\exp[(E-E_F)/k_BT]+1\}$ is the Fermi-Dirac distribution, $M(E) = \sum_{i=1}^{M} T_i(E)$ is the total transmission summed over all incoming modes in the input lead, and $G_0 = 2e^2/h$ is the conductance quantum.

III. RESULTS

A. Effect of disorder on the SGM maps

In Fig. 2(a), we show the scattering electron density for the smooth disorder at $T = 0$ K with dG/dx depicted in Fig. 2(b). A branched flow is formed far from the QPC with well visible $\lambda_F/2$ fringes [9]. Near the QPC, characteristic circular fringes [16] appear due to the standing wave between the QPC and the tip [see the backscattered trajectory in Fig. 1(a)]. Smooth defects lead to small-angle scattering and the branched flow remains straight over large distances. This kind of flow is found in the high-mobility samples [9].

Figure 2(c) shows the scattering electron density for the case of hard impurities. The potential centers (white dots) are superimposed on the electron density image in order to show the relation between the location of branches and impurity distribution within the sample. From this image, one notices that the two main branches are formed along the lines with a lower impurity density [one of those branches is denoted by the black arrow in Fig. 2(d)]. Not every impurity splits the electron flow in branches and the current passes across some of them.

Aside from the two dominating branches in Fig. 2(c), one can see a number of characteristic funnel-shaped fringe patterns denoted by the squares. Those patterns accompany the splitting of the electron density in two branches by a hard impurity in the branch. This process is schematically presented in Fig. 4(a) and can also be noted in Fig. 3(a). Due to the finite size of the obstacle, the electron has to flow around, which leads to the funnel-shaped local widening of the branch near the impurity. In the presence of the SGM tip, the electron waves can be backscattered within the funnel area [see Figs. 4(b) and 4(c)], which results in the characteristic circular fringes visible in Fig. 3(b). At some point when the tip depletion area does not block both parts of the split branches, backscattering is reduced and circular fringes disappear from the SGM images. The funnel-shaped fringe patterns are also visible in the experimental images, e.g., see Fig. 2(b) of Refs. [24] and [7]. Let us note that by analyzing the size of the circular fringes, one may roughly estimate the depletion radius d_{depl} induced by the SGM tip, as the distance between the funnel focal point and the last fringe in the funnel, i.e., the distance between tip location inducing the flow depicted in Figs. 4(b) and 4(d) (or points A and C in Fig. 3). From Fig. 3(b), we get an approximated value of depletion radius $d_{\mathrm{depl}} \approx 120$ nm. This value is of the order of the one obtained from condition $E_F = V_{\mathrm{tip}}$, which is

$$d_{\mathrm{depl}} = d_{\mathrm{tip}} \sqrt{\frac{V_t}{E_F} - 1} = 80 \text{ nm}. \qquad (4)$$

B. Thermal stability of the fringes

One of the most unexpected features of the branched flow in the disordered samples is the stability of the interference fringes against thermal broadening, which allows for observation of the fringes at several microns from the QPC at $T = 4$ K, when the thermal length is only $l_{\mathrm{th}} = \frac{2\pi\hbar^2}{m\lambda_F k_B T} = 400$ nm [6,7,9]. In Figs. 5(a)–5(c), we show the simulated SGM dG/dx maps for a system with hard impurities at $T = 0$, 1, and 4 K. The calculations here as well as subsequent later calculations are performed for a slightly smaller system than in Fig. 2 and the positions of the scatterers are changed, hence the difference in the SGM images.

Comparing both Figs. 5(c) and 5(d), one can see that the persistence of the interference fringes at high temperatures at large distances is directly caused by the disorder within the sample [6,7]. Additionally, a few other features can be found

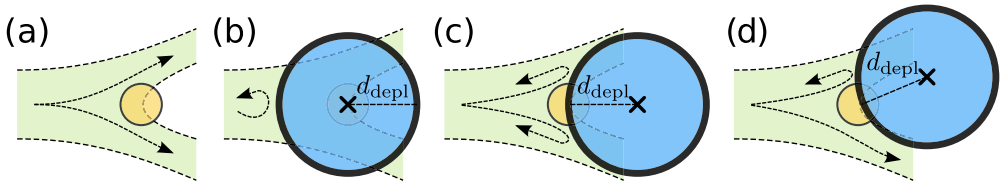

FIG. 4. Sketch of the scattering process leading to the funnel-shaped fringes in the SGM images. (a) Branched flow around impurity without SGM tip. (b) Tip is above impurity; (c) at the widest branch point when the tip still closes both paths; and (d) when the tip deletion area leaves the funnel-shaped branch around the impurity. The d_{depl} is the radius of the area depleted by the SGM tip.

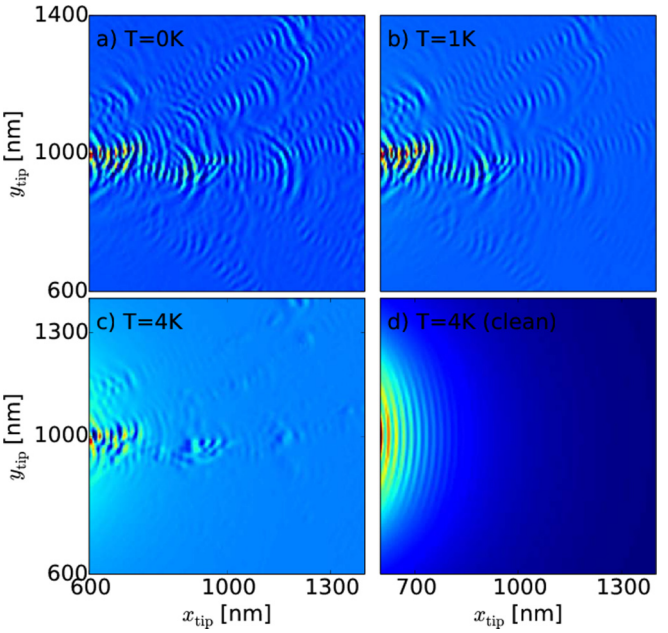

FIG. 5. (a)–(c) Simulated SGM images in the presence of disorder obtained at (a) $T = 0$, (b) $T = 1$, and (c) $T = 4$ K. (d) Same as (c), but without disorder. The quantity dG/dx is plotted in arbitrary units.

in the SGM images: (i) interference fringes are perpendicular to the flow direction, (ii) at 4 K, some fringes disappear for a short distance to reappear at a further distance, and (iii) in general, the fringe period is not uniform.

For the current flowing in branches, the transport across the 2D system can be reduced to the 1D scattering system provided that the current leakage from the branch and the branch splittings are neglected. We found that the observed features of the branches can be explained within a model in which the electron branch is treated as a one-dimensional electron channel. The perpendicular orientation of the fringes inside the branch is implied—see Appendix B.

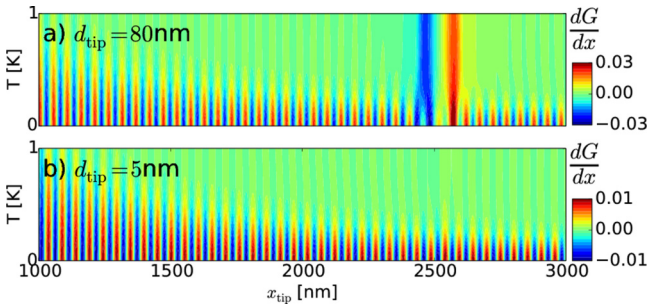

FIG. 7. (a) The temperature evolution of the dG/dx scan from Fig. 6(d). (b) Same as (a), but for narrower SGM potential width $d_{tip} = 5$ nm.

In Fig. 6(a), we show a 1D representation of a "clean" branch. An electron with kinetic energy $E_F = 3$ meV is incoming from the left reservoir and scatters on the QPC and SGM tip potentials inside the channel. We set $V_t = E_F$. The calculated SGM signal dG/dx is presented in Fig. 6(b) for $T = 0$ and 1 K. For $T = 1$ K, the interference fringes disappear as functions of tip position along the branch, which results from the finite width of the transport window near the Fermi level. The simulation for a single impurity within the channel [Fig. 6(c)] shows that the interference fringes reappear around the impurity [Fig. 6(d)]. This is possible when the distance between the SGM tip and the impurity becomes smaller than the thermal length [9]. The measured current is then sensitive to the interference which takes place far from the QPC; thus the presence of fringes in the SGM images at large distances is evidence of nearby impurities. In Figs. 6(e) and 6(f), we show that for a disordered channel, the fringes remain visible at large tip distances for $T = 1$ K, which results from the multiple scattering between tip and nearby impurities. This effect is more dramatic in the case of 2D scattering, where for $T = 4$ K in Fig. 5(c), the amplitude of the fringes at some points is reduced almost to zero. One may note that at some points,

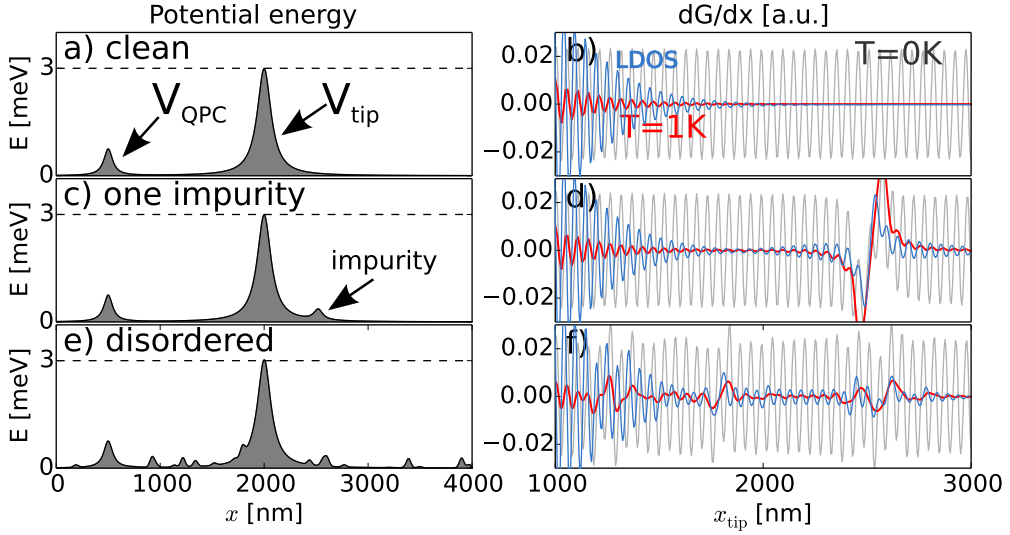

FIG. 6. (a) Potential-energy landscape for a clean 1D branch and (b) resulting dG/dx conductance for $T = 0$ and 1 K. (c), (d) Same as (a) and (b), but for the case of one impurity inside the channel and (e), (f) for a large number of impurities. The blue profiles in (b), (d), and (f) correspond to minus the x derivative of the local density of states ($-d\text{LDOS}/dx$) inside the branch without the SGM tip at $T = 1$ K.

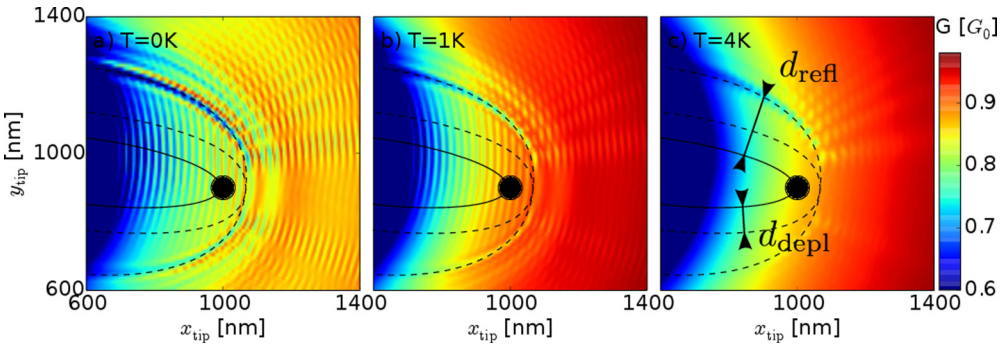

FIG. 8. (a) Simulated SGM image obtained for $T = 0$ and one hard impurity in the system with position denoted by a circle. (b) Same as (a), but for $T = 1$ K and (c) $T = 4$ K. The smallest ellipse is calculated from condition $r_{q-t-i} - r_{q-i} = \lambda_F/2$. The middle ellipse is the smallest one enlarged by d_{depl} along the normal direction. The largest contour is calculated from the correction on the finite size of the tip depletion radius and the scattering angle from Eq. (6).

temperature does change the period of the fringes around the impurities in Fig. 6(f); however, the period of the fringes in the spatial derivative of the local density of states (LDOS) without SGM tip [see blue lines in Figs. 6(b), 6(d), and 6(f)] remains constant in comparison to the dG/dx signal. This observation suggests that the change of the fringes' period is directly caused by the SGM tip itself. The nonuniformity of the fringe spacing at finite temperature was experimentally observed, for instance, in Fig. 4 of Ref. [8] and in Fig. 7 of Ref. [25]. One should also note the high correlation between dG/dx and $d\mathrm{LDOS}/dx$ in each of the cases in Figs. 6(b), 6(d), and 6(f).

In Fig. 7(a), we show the temperature evolution of the dG/dx scan from Fig. 6(d). Far from the QPC and the impurity (located at $x = 2500$ nm), the decay of the interference fringes with increasing T is well visible and the period of the fringes remains constant. This is, however, not the case around the impurity, since (1) we observe a rapid change of period with T and (2) the amplitude of the fringes in the vicinity of the impurity varies much slower than for usual fringes. The latter feature is also visible in 2D simulations in Fig. 5. In Fig. 7(b), we show the same scan as in Fig. 7(a), but for a narrower SGM tip, i.e., $d_{\mathrm{tip}} = 5$ nm. Note that in this case, the position of the impurity is almost undetectable, which shows the importance of the spatial width of the SGM tip on the fringes' period, i.e., only the wide tip does change the fringe frequency.

C. A single hard scatterer in a high-mobility sample

Another interesting and previously unexplored interference scenario takes place in high-mobility samples when a small number of hard impurities is present. In Figs. 8(a)–8(c), we show SGM images for a single hard impurity within the device (with position marked by the black dot) for temperatures $T = 0$, 1, and 4 K. The characteristic quasielliptic fringes visible in the SGM images can be explained as a result of the interference between electron waves following two different paths between the QPC and the impurity: (i) a direct path of length r_{q-i} and (ii) a path of length $r_{q-t-i} = r_{q-t} + r_{t-i}$ induced by the reflection on the depleted area below the tip [see Fig. 9(a)]. When the length difference is an integer multiple of the Fermi wavelength, the interference is constructive at the impurity location, resulting in a stronger backscattering and a lower conductance. The resulting interference fringes can be approximated as

$$G \propto -\cos[k_F(r_{q-t-i} - r_{q-i})]. \tag{5}$$

The map calculated from Eq. (5) is presented in Fig. 9(b) and it can be compared with Fig. 9(c), where we show the SGM image calculated for a pointlike tip ($d_{\mathrm{tip}} = 5$ nm and $V_t = 5E_F$ such that $d_{\mathrm{depl}} = 10$ nm). The white dashed lines in Figs. 9(b) and 9(c) represent the isolines for $r_{q-t-i} - r_{q-i} =$

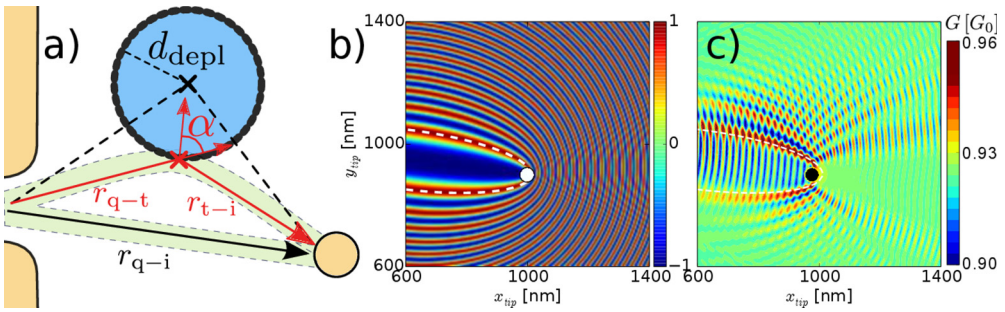

FIG. 9. (a) Two paths which lead to the elliptic fringe pattern displayed in (b). The blue disk is the 2DEG depleted area beneath the tip. The orange dot is the hard scatterer. The dashed lines show an effective shift of the tip position that is due to the finite size of the depletion area and α is the angle of incidence of the electron wave to the depleted area. (b) The elliptic fringes obtained from Eq. (5). (c) The SGM image obtained for a simulation using a pointlike tip potential with $d_{\mathrm{tip}} = 5$ nm and $V_t = 5E_F$.

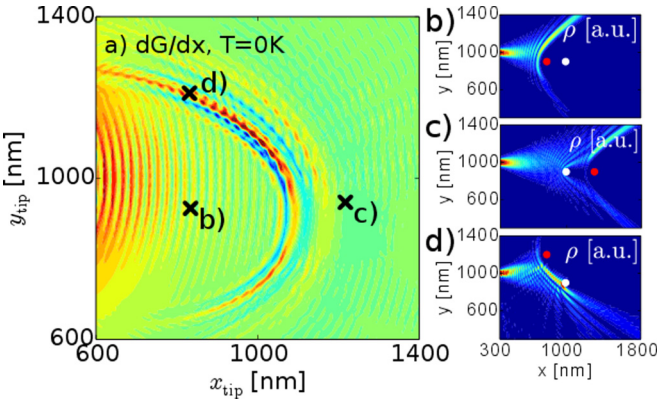

FIG. 10. (a) Same as in Fig. 8(a), but dG/dx image. (b)–(d) Scattering electron densities obtained for tip positions denoted by crosses in (a). The white dot is the impurity and the red dot is the tip position.

$\lambda_F/2$, i.e., the position of the tip leading to the first destructive interference between the paths marked in Fig. 8(a).

In Figs. 10(c) and 10(d), we show the scattering probability densities that are at the origin of subsequent interference fringes visible in SGM images in Fig. 10(a) or in Fig. 8(a). The circular fringes visible inside the ellipse [see Fig. 10(b)] are characteristic of a clean impurity-free sample and appear for the impurity hidden by the tip depletion area [as in Fig. 5(d)]. On the other hand, in Fig. 10(c), the tip is located in the shadow of the impurity, which results in strongly suppressed fringes since very small electron flow arrives to the tip and thus the conductance map weakly depends on the tip position. In other tip positions [as in Fig. 9(d)], the process involves both the impurity and the tip [cf. Fig. 9(a)] producing the elliptic fringes.

From Fig. 8(c), one can see that the elliptic pattern is thermally more stable than the circular fringes which decay rapidly with the distance to the QPC. The most stable elliptic fringe is the one for which the length difference between two paths in Fig. 9(a), $r_{q-i} - r_{q-t-i}$, is equal to half the Fermi wavelength ($\lambda_F/2 = 27.35$ nm)—which is much shorter than the thermal length.

In order to explain the exact position of the first elliptic fringe, one needs to account for the finite size of the depletion area and the electron incidence angle α to the depletion area [see Fig. 8(a)]. Since the kinetic energy related to the electron motion in the direction normal to the tip equipotential lines is $E_F \cos(\alpha)$, the reflection point is located at a distance d_{refl} from the tip given by $E_F \cos(\alpha) = V_{tip}(r = d_{refl}) = eV_t d_{tip}^2/(d_{tip}^2 + d_{depl}^2)$. From this condition, one derives the reflection radius,

$$d_{refl} = d_{tip}\sqrt{\frac{eV_t}{E_F \cos(\alpha)} - 1}, \tag{6}$$

which equals the depletion radius d_{depl} (4) for the normal incidence, $\alpha = 0$, but is much larger for higher incidence angles. In Figs. 8(a)–8(c), three lines have been drawn on the SGM images: (i) the solid line is an ellipse corresponding to the first interference fringe for a pointlike tip potential and denotes the first interference fringe [same as white dashed lines in Figs. 9(b) and 9(c)]; (ii) the central ellipse corresponds to the smallest ellipse simply enlarged by d_{depl} in the normal direction; and (iii) the largest contour corresponds to the smallest ellipse but enlarged by d_{refl} from Eq. (6) in the normal direction. This contour is no longer an ellipse and we refer to this kind of curve as quasielliptic/ellipse (QE) in the following. In order to fit this model to the SGM image, we have set $d_{tip} = 75$ nm in Eq. (6), which is about the nominal value of 80 nm. We have to slightly move the impurity location by 20 nm to the left, which is of the order of the impurity radius. The idea of the incidence-angle-dependent penetration depth was employed in a recent work of Ref. [26] in which the authors analyzed small-angle scattering trajectories induced by potential barriers lower than the Fermi energy.

Figures 11(a)–11(c) show SGM images for three hard impurities in the system with a set of QE fringes. The dashed lines show QEs obtained from Eq. (6) with $d_{tip} = 75$ nm, which agree with the value used in the simulation. Note that for a few hard impurities, the SGM images resolve the QE fringes resulting from separate interference scenarios.

D. Experimental maps for hard scatterers

For the experiment, we use the same series of samples as in Refs. [4,27] for which the interference fringes between the QPC and the tip—independently of the hard scatterers—were reported previously at low temperature. The presence of hard scatterers can be more easily identified in SGM images recorded at a higher temperature, for which the "clean" interference fringes disappear. In this section, we

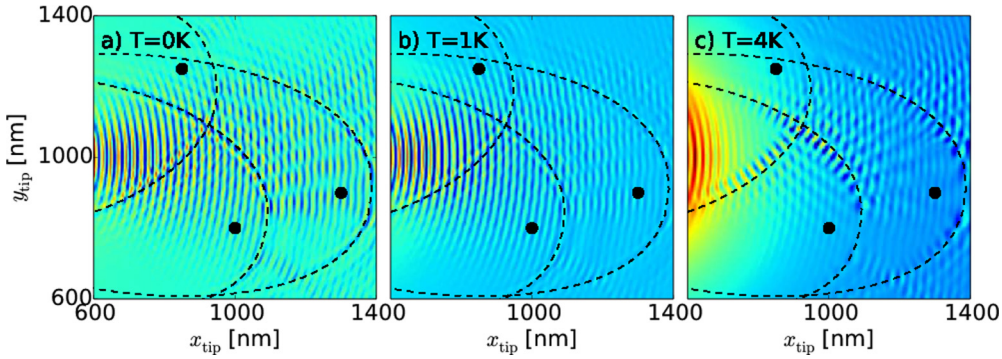

FIG. 11. (a)–(c) Simulated dG/dx SGM images (in arbitrary units) similar to those in Figs. 8(a)–8(c), but for three hard impurities denoted by dots. Dashed lines present the calculated position of the first fringe from Eq. (6).

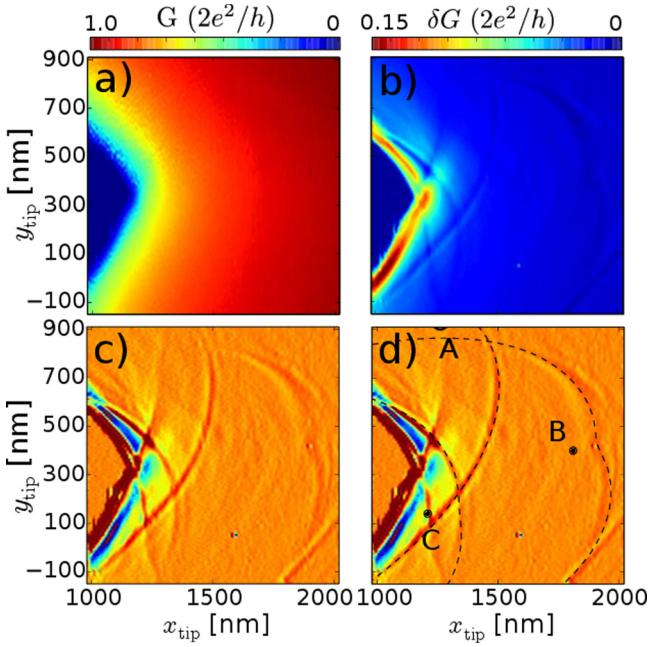

FIG. 12. (a) Experimental SGM image of the conductance as a function of the tip position for a tip voltage of −6 V. (b) SGM image of the transconductance, i.e., the response of the conductance to a 50 mV ac modulation applied to the tip around its dc value of −6 V. The data plotted in (a) and (b) are measured simultaneously. The origin of the coordinates is the center of the QPC. (c) Numerical derivative of (b) with respect to the horizontal axis, giving higher contrast to the lines. (d) The dashed lines show the theoretical tip position of the first fringe calculated for the three impurity positions indicated by the dots (A,B,C) with Eq. (6) with $\frac{eV_t}{E_F} = 1.2$ and $d_{tip} = 200$ nm for points A and B, and $\frac{eV_t}{E_F} = 1.5$, $d_{tip} = 170$ nm for point C.

illustrate the effects of single hard scatterers in a high-mobility sample by discussing a SGM experiment performed at 4.2 K. The QPC is defined in a 2DEG located 105 nm below the surface of a GaAs/AlGaAs heterostructure. The 2DEG has a 2.5×10^{11} cm^{-2} electron density and a 1.0×10^{6} cm^2 V^{-1} s^{-1} electron mobility [4,27]. The QPC is defined by a Ti/Au split gate whose rectangular gap is 350 nm wide and 200 nm long. The device is mounted in a cryogenic scanning probe microscope and cooled down to a temperature of 4.2 K. The tip of the SGM microscope is a commercial platinum-coated AFM tip fixed with silver epoxy to a tuning fork which is used as the force sensor for topographic imaging. In the SGM mode, the tip is scanned above the 2DEG with a constant tip voltage of −6 V and a tip-to-surface distance of 35 nm. The QPC gate voltage is kept fixed at −0.8 V in order to have the QPC conductance equal to one conductance quantum $2e^2/h$ when the tip is far from the QPC. To enhance the sensitivity of the measurement to small tip-induced effects, a small ac voltage modulation is applied to the tip and the demodulated current response gives a transconductance signal. The conductance $G = I^{ac}/V^{ac}_{bias}$ is measured with a 100 μV ac bias voltage applied between source and drain, while the transconductance $\delta G = I^{ac}/V^{dc}_{bias}$ is measured with a 50 mV ac voltage applied to the tip and a 150 μV dc bias voltage applied between source and drain. The current flowing through the QPC is amplified and the response to the ac excitation is measured with a lock-in technique.

The SGM images plotted in Figs. 12(a) and 12(b) present the conductance and transconductance signals as a function of the tip position. The center of the QPC is located at coordinates (0,0) as determined by SGM images recorded above the QPC and higher tip-to-surface distance (data not shown). While the conductance image simply shows the gating effect of the tip on the QPC transmission, the transconductance image shows several additional lines. The origin of these lines is attributed to the presence of hard scatterers in the 2DEG, as discussed above in Sec. III C.

In the following discussion, we assume that the lines arise from a single hard scatterer, although we are aware of the possibility that more impurities are involved. The dashed lines in Fig. 12(d) show QEs fitted using Eq. (6) in which we employ $\frac{V_t}{E_F} = 1.2$ and $d_{tip} = 200$ nm for the impurities A and B. In order to fit Eq. (6) to fringes originating from impurities A and B, we set position of the QPC to $r_{QPC} = (50,-100)$ nm, $r_A = (1260,920)$ nm, and $r_B = (1810,400)$ nm. Note that the QPC position obtained from the fit is shifted with respect to the center of the QPC [nominally (0,0)], which results from the fact that the interference result from scattering between the tip and the QPC gates—and not the QPC entrance [10]—and thus the QPC focal point of the QE is not located at the entrance of the QPC. At the scale of Fig. 11, the shift of r_{QPC} from the origin is small anyway. For the impurity C, we get slightly different values, $\frac{V_t}{E_F} = 1.5$, $d_{tip} = 170$ nm, $r_{QPC} = (0,50)$ nm, and $r_C = (1210,140)$ nm. The difference in the tip potential parameters may be due to the screening of the tip by the gates (C is closer to the gates than A and B). The observed number of impurities in the scanned area 1×1 μm gives impurity density $n_{imp} \approx 3$ $(\frac{1}{\mu m^2})$, which can be used to roughly estimate the electron mobility inside the 2DEG with semiclassical formula $\mu = \frac{ql_p}{\sqrt{2mE_F}} = \frac{q\lambda_F l_p}{h}$, where $l_p = 1/n_{imp}\lambda_F$ is the mean free path. The value of l_p is estimated from the semiclassical Broglie's assumption of the electron being a particle of diameter λ_F colliding with pointlike scatters uniformly distributed in the sample. The approximated expression for electron mobility reduces then to the simple formula $\mu = \frac{q}{n_{imp}h} \approx 0.8\times10^{6}$ cm^2 V^{-1} s^{-1}.

The evolution of the lines with the tip voltage is presented in Figs. 13(a)–13(e). When the tip voltage is made more negative, the lines move to larger distances from the QPC and become wider in the transverse direction (smaller curvature). This behavior is consistent with the simulations presented in Fig. 8(c), where a larger depletion disk below the tip results in a lower eccentricity of the QE lines. The dashed lines in Figs. 13 show the results of Eq. (6) that are obtained with increasing values of $d_{tip} = \{165,205,235,260,280\}$ nm and ratio $\frac{V_t}{E_F} = \{1.19,1.22,1.3,1.4,1.45\}$, respectively. This nontrivial evolution of the tip-induced potential parameters (nonconstant d_{tip} and slowly varying V_t) reflects the complex behavior of the nonlinear screening in the case of partial depletion. We obtain a change of the tip radius to be about ∼30 nm for a 1 V change on the tip. In order to obtain a good fit between the first QE lines and the analytical expression, we shift the positions of the impurity in Figs. 13(b)–13(e) (filled circles) with respect to the calculated position in the

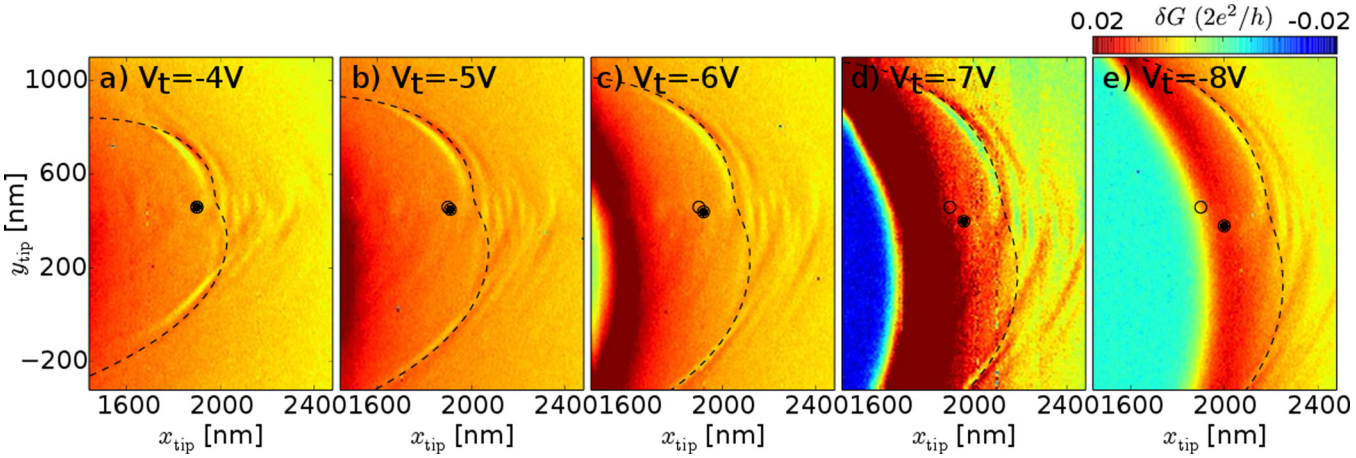

FIG. 13. Experimental SGM images of the transconductance for different tip voltages: (a) −4, (b) −5, (c) −6, (d) −7, and (e) −8 V. In addition to the increasing gating effect, the lines due to the presence of hard scatterers moves to the right and change in curvature. Note that these images have been recorded for a slightly smaller QPC transmission than in Fig. 12, resulting in a faster closing of the QPC channel. The filled dots show the assumed position of the impurity, while the empty dots indicate the impurity position in (a). Dashed lines represent the theoretical tip position of the first fringe calculated from Eq. (6).

first image of Fig. 13(a) (empty circles) by about (20, −20 nm) per image. The reason for this shift may be caused by the drift of the sample with respect to the tip position due to the long acquisition time of $2\frac{1}{2}$ h per image.

IV. SUMMARY AND CONCLUSIONS

To summarize, we have discussed the role of smooth and hard impurities in the 2DEG on the SGM images. We have shown that the funnel-like features that appear in conductance maps result from the splitting of the branches by hard impurities, and the position of the impurity is always shifted in the SGM images due to the finite size of the depletion area. We have shown that a 1D interpretation of branches can be used to explain most of the features present in the conductance maps, including their thermal stability. Additionally, we have discussed that in the presence of a small number of hard impurities in a high-mobility sample, characteristic quasielliptic fringes can be found in the SGM images even at reasonably high temperatures, ∼4 K. We have explained those findings in terms of interference between two paths involving both the tip and the impurity with length difference of the order of $\lambda_F/2$. We have provided experimental evidence for these interference processes as well as a simple analytical formula which can be used to extract the position of the impurity and to estimate the depletion radius due to the tip. A reliable estimation of the depletion radius for fixed SGM parameters needs to account for the dependence of the effective width of the tip potential on the scattering angle.

ACKNOWLEDGMENTS

This work was supported by the National Science Centre according to Grant No. DEC- 2015/17/N/ST3/02266 and by the PL-Grid Infrastructure. K.K. is financially supported by a scholarship of the Krakow Smoluchowski Scientific Consortium from the funding for the National Leading Research Centre by Ministry of Science and Higher Education (Poland) and by the Etiuda stipend of the National Science Centre (NCN) according to Grant No. DEC-2015/16/T/ST3/00310. The experimental work was supported by the French Agence Nationale de la Recherche ("ITEM-exp" project) and the sample fabrication was done by U. Gennser and D. Mailly from CNRS/LPN.

APPENDIX A: DESCRIPTION OF THE NUMERICAL METHOD

We start from the derivation of the scattering boundary conditions using the approach from Ref. [28]. Let us assume that the simulated device can be approximated by tight binding, such as Hamiltonian $\boldsymbol{H}$. In our case, such Hamiltonian is generated from a finite-difference approximation of the derivatives of the differential operators in $\boldsymbol{H}$ [29]. Additionally, we follow Ref. [21] and we divide the system into consecutive slices $\boldsymbol{H}_i$ connected by coupling matrices $\boldsymbol{\tau}_i$, forming block-tridiagonal systems of linear equations for the scattering wave function $\boldsymbol{c}$ inside the system,

$$-\boldsymbol{\tau}_{i-1}\boldsymbol{c}_{i-1} + (E_F - \boldsymbol{H}_i)\boldsymbol{c}_i - \boldsymbol{\tau}_i^\dagger \boldsymbol{c}_{i+1} = 0.$$

In the lead region (semi-infinite lead can be located in any part of the system), the system is assumed to be homogeneous, and thus one may drop the indices in the matrices and write

$$-\boldsymbol{\tau}\boldsymbol{c}_{i-1} + (E_F - \boldsymbol{H})\boldsymbol{c}_i - \boldsymbol{\tau}^\dagger \boldsymbol{c}_{i+1} = 0, \tag{A1}$$

which can be solved by Bloch substitution $\boldsymbol{c}_n = \lambda^n \boldsymbol{u}$ [21], leading to quadratic eigenvalue equation for the transverse modes [21,22],

$$-\boldsymbol{\tau}\boldsymbol{u} + \lambda(E_F - \boldsymbol{H})\boldsymbol{u} - \lambda^2\boldsymbol{\tau}^\dagger\boldsymbol{u} = 0,$$

which can be transformed to a generalized eigenvalue problem (GEP) of double size,

$$\begin{pmatrix} \boldsymbol{0} & \boldsymbol{1} \\ -\boldsymbol{\tau} & E_F - \boldsymbol{H} \end{pmatrix}\begin{pmatrix} \boldsymbol{u} \\ \lambda\boldsymbol{u} \end{pmatrix} = \lambda\begin{pmatrix} \boldsymbol{1} & \boldsymbol{0} \\ \boldsymbol{0} & \boldsymbol{\tau}^\dagger \end{pmatrix}\begin{pmatrix} \boldsymbol{u} \\ \lambda\boldsymbol{u} \end{pmatrix}. \tag{A2}$$

We solve it numerically by converting it to a standard eigenvalue problem (SEP), since in our case $\boldsymbol{\tau}^\dagger$ is invertible.

If $\boldsymbol{\tau}^\dagger$ is noninvertible or ill conditioned, one may use more sophisticated methods which incorporate singular-value decomposition (SVD) of the $\boldsymbol{\tau}^\dagger$ matrix [30].

The eigenvalues of the equation above are then grouped into incoming $\{\lambda_{m,+},\boldsymbol{u}_{m,+}\}$ and outgoing $\{\lambda_{m,-},\boldsymbol{u}_{m,-}\}$ modes, with each propagating mode $\boldsymbol{u}_{m,\pm}$ (i.e., with $|\lambda_{m,\pm}| = 1$) normalized to carry the unit value of quantum flux. For a more detailed description, see [21].

The solution in the semi-infinite lead for the mth incoming mode can be expressed in terms of superposition transverse modes,

$$\boldsymbol{c}_n = \lambda_{m,+}^n \boldsymbol{u}_{m,+} + \sum_{k=1}^{N} r_k \lambda_{k,-}^n \boldsymbol{u}_{k,-}, \tag{A3}$$

where $\lambda_{m,+}^n$ is the Bloch factor [21] for the mth incoming mode $\boldsymbol{u}_{m,+}$ and N is the number of sites in the lead slice, i.e., the size of the vector $\boldsymbol{u}_{k,\pm}$. Vector $\boldsymbol{u}_{k,-}$ denotes the kth outgoing mode. For a more detailed description of how the transverse modes are calculated, see Ref. [21]. By choosing the frame of coordinates such that $i = 0$ denotes the first slice in the considered system, one may expand the wave function at this slice in terms of transverse modes,

$$\boldsymbol{c}_0 = \boldsymbol{u}_{m,+} + \sum_{k=1}^{N} r_k \boldsymbol{u}_{k,-}; \tag{A4}$$

note that $\boldsymbol{c}_0$ is now a part of the discretized system. By projecting $\langle \boldsymbol{u}_{p,-}|$ on Eq. (A4), we get

$$\langle \boldsymbol{u}_{p,-}|\boldsymbol{c}_0\rangle = \langle \boldsymbol{u}_{p,-}|\boldsymbol{u}_{m,+}\rangle + \sum_{k=1}^{N} r_k \langle \boldsymbol{u}_{p,-}|\boldsymbol{u}_{k,-}\rangle,$$

with $\langle a|b\rangle = \sum_k^N a^*(k)b(k)$, which can be written in terms of matrices,

$$\boldsymbol{r} = \boldsymbol{S}(\boldsymbol{Q} - \boldsymbol{B}_m),$$

with $\boldsymbol{r}=\{r_1,r_2,\ldots,r_N\}$, $\boldsymbol{Q}_p=\langle \boldsymbol{u}_{p,-}|\boldsymbol{c}_0\rangle$, $\boldsymbol{B}_{m,p}=\langle \boldsymbol{u}_{p,-}|\boldsymbol{u}_{m,+}\rangle$, and $S_{p,k}^{-1} = \langle \boldsymbol{u}_{p,-}|\boldsymbol{u}_{k,-}\rangle$. Additionally, by forcing the derivative of the wave function to be continuous at the device boundary, we obtain the second condition,

$$\boldsymbol{c}_0 - \boldsymbol{c}_{-1} = \left(1 - \lambda_{m,+}^{-1}\right)\boldsymbol{u}_{m,+} + \sum_{k=1}^{N}\left(1 - \lambda_{k,-}^{-1}\right) r_k \boldsymbol{u}_{k,-}.$$

Then, by substituting the $\boldsymbol{r}$ vector to the equation above, we get

$$\begin{aligned}\boldsymbol{c}_0 - \boldsymbol{c}_{-1} &= \left(1 - \lambda_{m,+}^{-1}\right)\boldsymbol{u}_{m,+} \\ &\quad + \sum_{k,p=1}^{N}\left(1 - \lambda_{k,-}^{-1}\right) S_{k,p}(Q_p - B_{m,p})\boldsymbol{u}_{k,-}.\end{aligned}$$

Let us now simplify the expression above, by starting from the first term in the sum on the right side,

$$\begin{aligned}&\sum_{k,p=1}^{N}\left(1 - \lambda_{k,-}^{-1}\right) S_{\mathrm{k,p}} Q_{\mathrm{p}} \boldsymbol{u}_{k,-} \\ &= \sum_{k,p=1}^{N}\left(1 - \lambda_{k,-}^{-1}\right) S_{k,p} \langle \boldsymbol{u}_{p,-}|\boldsymbol{c}_0\rangle \boldsymbol{u}_{k,-} \\ &= \sum_{k,p=1}^{N}\left(1 - \lambda_{k,-}^{-1}\right) S_{k,p} \sum_{i}^{N} u_{p,-}^*(i) c_0(i) \boldsymbol{u}_{k,-} \\ &= \sum_{i,k,p=1}^{N} \boldsymbol{u}_{k,-}\left(1 - \lambda_{k,-}^{-1}\right) S_{k,p} u_{p,-}^*(i) c_0(i) \\ &= \boldsymbol{U}_-\left(\mathbf{1} - \boldsymbol{\Lambda}_-^{-1}\right)\boldsymbol{S}\boldsymbol{U}_-^\dagger \boldsymbol{c}_0,\end{aligned}$$

where columns of matrix $\boldsymbol{U}_\pm$ are constructed from transverse modes $\boldsymbol{U}_\pm = (|\boldsymbol{u}_{1,\pm}\rangle, |\boldsymbol{u}_{2,\pm}\rangle, \ldots, |\boldsymbol{u}_{N,\pm}\rangle)$ and $\Lambda_{i,j,\pm} = \delta_{i,j}\lambda_{i,\pm}$. Analogously for the second term, we obtain

$$\sum_{k,p=1}^{N}\left(1 - \lambda_{k,-}^{-1}\right) S_{k,p} B_{m,p} \boldsymbol{u}_{k,-} = \boldsymbol{U}_-(\mathbf{1} - \boldsymbol{\Lambda}_-^{-1})\boldsymbol{S}\boldsymbol{U}_-^\dagger \boldsymbol{u}_{m,+}.$$

Thus we get

$$\begin{aligned}\boldsymbol{c}_0 - \boldsymbol{c}_{-1} &= \left(1 - \lambda_{m,+}^{-1}\right)\boldsymbol{u}_{m,+} + \boldsymbol{U}_-(\mathbf{1} - \boldsymbol{\Lambda}_-^{-1})\boldsymbol{S}\boldsymbol{U}_-^\dagger \boldsymbol{c}_0 \\ &\quad - \boldsymbol{U}_-(\mathbf{1} - \boldsymbol{\Lambda}_-^{-1})\boldsymbol{S}\boldsymbol{U}_-^\dagger \boldsymbol{u}_{m,+}.\end{aligned} \tag{A5}$$

The expression above can be further simplified by noticing that $\boldsymbol{S} = (\boldsymbol{U}_-^\dagger \boldsymbol{U}_-)^{-1} = \boldsymbol{U}_-^{-1}(\boldsymbol{U}_-^\dagger)^{-1}$, hence the matrix

$$\begin{aligned}\boldsymbol{U}_-(\mathbf{1} - \boldsymbol{\Lambda}_-^{-1})\boldsymbol{S}\boldsymbol{U}_-^\dagger &= \boldsymbol{U}_-(\mathbf{1} - \boldsymbol{\Lambda}_-^{-1})\boldsymbol{U}_-^{-1}(\boldsymbol{U}_-^\dagger)^{-1}\boldsymbol{U}_-^\dagger \\ &= \mathbf{1} - \boldsymbol{U}_-\boldsymbol{\Lambda}_-^{-1}\boldsymbol{U}_-^{-1} \equiv \mathbf{1} - \boldsymbol{F}_-.\end{aligned}$$

The matrix $\boldsymbol{F}_\pm \equiv \boldsymbol{U}_\pm(\boldsymbol{U}_\pm\boldsymbol{\Lambda}_\pm)^{-1}$ is the Bloch matrix. The final formula for Eq. (A5) is then

$$\boldsymbol{c}_{-1} = \boldsymbol{F}_-\boldsymbol{c}_0 + \left(\lambda_{m,+}^{-1}\mathbf{1} - \boldsymbol{F}_-\right)\boldsymbol{u}_{m,+}.$$

By inserting this into the Hamiltonian (A1) for $i = 0$, one removes the dependence of the $\boldsymbol{c}_{-1}$ slice from the linear system, which gives

$$(E_\mathrm{F} - \boldsymbol{H} - \boldsymbol{\tau}\boldsymbol{F}_-)\boldsymbol{c}_0 - \boldsymbol{\tau}^\dagger \boldsymbol{c}_1 = \boldsymbol{\tau}\left(\lambda_{m,+}^{-1}\mathbf{1} - \boldsymbol{F}_-\right)\boldsymbol{u}_{m,+}.$$

We note that

$$\begin{aligned}\boldsymbol{F}_+|\boldsymbol{u}_{m,+}\rangle &= \boldsymbol{U}_+\boldsymbol{\Lambda}_+^{-1}\boldsymbol{U}_+^{-1}|\boldsymbol{u}_{m,+}\rangle \\ &= \boldsymbol{U}_+|0,\ldots,\lambda_{m,+}^{-1},\ldots,0\rangle \\ &= \lambda_{m,+}^{-1}|\boldsymbol{u}_{m,+}\rangle,\end{aligned}$$

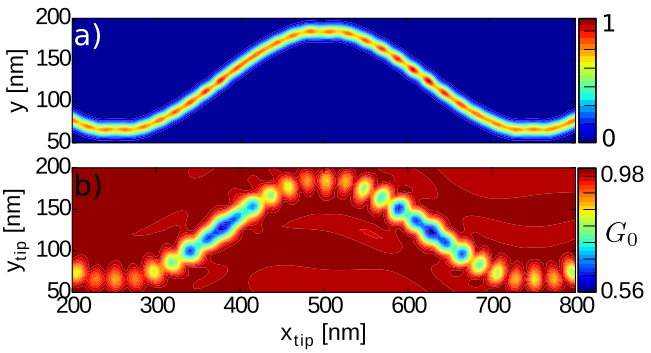

FIG. 14. (a) Scattering density inside the sinus-shaped channel. The Fermi level corresponds to a single conducting mode. (b) The SGM image of (a). We use $d_\mathrm{tip} = 40$ nm and $V_t = \frac{1}{2}E_\mathrm{F}$.

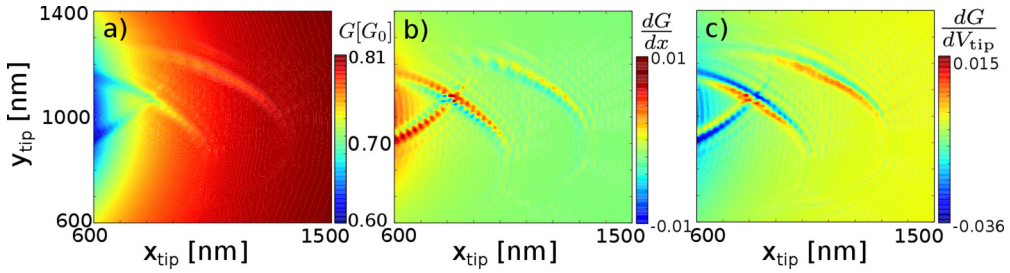

FIG. 15. (a) Simulated SGM conductance image of system with three impurities. (b) The spatial derivative of (a). (c) The transconductance image $dG/dV_{\rm tip}$ in arbitrary units.

and hence the right side can be written in a more compact form,

$$\boldsymbol{\tau}\left(\lambda_{m,+}^{-1}\mathbf{1}-\boldsymbol{F}_{-}\right)|\boldsymbol{u}_{m,+}\rangle=\boldsymbol{\tau}(\boldsymbol{F}_{+}-\boldsymbol{F}_{-})\,|\boldsymbol{u}_{m,+}\rangle\equiv\Gamma_{m}.$$

A summary of the system of linear equations for the case of a two-terminal device can be written in the following way:

$$[E_{\rm F}-(\boldsymbol{H}_0+\boldsymbol{\Sigma}_0)]\boldsymbol{c}_0-\boldsymbol{\tau}_0^{\dagger}\boldsymbol{c}_2=\boldsymbol{\Gamma}_{0,m},\tag{A6}$$

$$-\boldsymbol{\tau}_{i-1}\boldsymbol{c}_{i-1}+(E_{\rm F}-\boldsymbol{H}_i)\boldsymbol{c}_i-\boldsymbol{\tau}_i^{\dagger}\boldsymbol{c}_{i+1}=0,\quad \text{for } 0<i<N,\tag{A7}$$

$$[E_{\rm F}-(\boldsymbol{H}_N+\boldsymbol{\Sigma}_N)]\boldsymbol{c}_N-\boldsymbol{\tau}_{N-1}\boldsymbol{c}_{N-1}=0,\tag{A8}$$

where $\Sigma_{0/N}=\boldsymbol{\tau}\boldsymbol{F}_{-}$ is the self-energy calculated for the left/right lead. Note that in order to obtain open boundary conditions, we use the approach from the quantum transmitting boundary method (QTBM) introduced in Ref. [28], but at the end we finish with the wave-function matching (WFM) equations [21], which shows that both methods are algebraically equivalent.

After solution of the scattering problem for a given mth incoming mode, one may calculate transmission amplitudes from

$$\boldsymbol{t}_m=\boldsymbol{U}_{N,-}^{-1}\boldsymbol{c}_{N,m},\tag{A9}$$

and reflection amplitudes as

$$\boldsymbol{r}_m=\boldsymbol{U}_{0,-}^{-1}(\boldsymbol{c}_{0,m}-\boldsymbol{u}_{m,+}),\tag{A10}$$

with $\boldsymbol{U}_{0,-}$ and $\boldsymbol{U}_{N,-}$ being the outgoing modes' matrices for the input and output lead, respectively.

APPENDIX B: ALIGNMENT OF THE FRINGES IN QUASI-1D CASE

In Sec. III B, we discuss the properties of branched flow in terms of 1D channels which carry most of the current in the structure. In that approximation, most of the features which are present in 2D simulations can be explained; however, the perpendicularity of the fringes, which is a 2D property of the electron flow, cannot be easily attributed to the strictly 1D model. In order to support our discussion, we perform a SGM simulation of a curved quasi-1D channel for which the scattering electron density is presented in Fig. 14(a). The quasi-1D transport is obtained by choosing the transverse confinement of the curved channel to carry only one mode. The SGM image for this case is depicted in Fig. 14(b) with well-visible perpendicularly aligned fringes.

APPENDIX C: THE TRANSCONDUCTANCE IMAGES

The results presented in the experimental part of this paper discuss the elliptic fringes visible in the transconductance images, $dG/dV_{\rm tip}$. However, in the numerical part, we restrict our data to simple gradients $\frac{dG}{dx}$ of conductance maps. In principle, both quantities correspond to two different measurements: the former measures the response of the system to the SGM tip potential change and the latter simply removes a slowly varying background from the SGM images as a high-pass filter.

The experimental measurements of G and transconductance are performed with either an ac or dc bias, respectively. The ac voltage heats the sample, which is not the case for dc measurements, and hence the fine details are usually resolved more clearly in transconductance plots. This is the case for the elliptical features of Fig. 12, which are only resolved in the transconductance plot.

For the model calculations, we find that both differentiation over $V_{\rm tip}$ and the $x_{\rm tip}$ give similar images (see Figs. 15 for comparison), so we restrict the calculations to $\frac{dG}{dx}$, which requires evaluation of a single conductance map only and is thus computationally cheaper.

[1] M. A. Eriksson, R. G. Beck, M. Topinka, J. A. Katine, R. M. Westervelt, K. L. Campman, and A. C. Gossard, Appl. Phys. Lett. **69**, 671 (1996).

[2] H. Sellier, B. Hackens, M. G. Pala, F. Martins, S. Baltazar, X. Wallart, L. Desplanque, V. Bayot, and S. Huant, Semicond. Sci. Technol. **26**, 064008 (2011).

[3] D. K. Ferry, A. M. Burke, R. Akis, R. Brunner, T. E. Day, R. Meisels, F. Kuchar, J. P. Bird, and B. R. Bennett, Semicond. Sci. Tech. **26**, 043001 (2011).

[4] B. Brun, F. Martins, S. Faniel, B. Hackens, G. Bachelier, A. Cavanna, C. Ulysse, A. Ouerghi, U. Gennser, D. Mailly, S. Huant, V. Bayot, M. Sanquer, and H. Sellier, Nat. Commun. **5**, 4290 (2014).

[5] B. J. van Wees, H. van Houten, C. W. J. Beenakker, J. G. Williamson, L. P. Kouwenhoven, D. van der Marel, and C. T. Foxon, Phys. Rev. Lett. **60**, 848 (1988).
[6] M. A. Topinka, B. J. LeRoy, S. E. J. Shaw, E. J. Heller, R. M. Westervelt, K. D. Maranowski, and A. C. Gossard, Science **289**, 2323 (2000).
[7] M. A. Topinka, B. J. LeRoy, R. M. Westervelt, S. E. J. Shaw, R. Fleischmann, E. J. Heller, K. D. Maranowski, and A. C. Gossard, Nature (London) **410**, 183 (2001).
[8] A. A. Kozikov, R. Steinacher, C. Rössler, T. Ihn, K. Ensslin, C. Reichl, and W. Wegscheider, Nano Lett. **15**, 7994 (2015).
[9] M. P. Jura, M. A. Topinka, L. Urban, A. Yazdani, H. Shtrikman, L. N. Pfeiffer, K. W. West, and D. Goldhaber-Gordon, Nat. Phys. **3**, 841 (2007)
[10] M. P. Jura, M. A. Topinka, M. Grobis, L. N. Pfeiffer, K. W. West, and D. Goldhaber-Gordon, Phys. Rev. B **80**, 041303 (2009).
[11] M. Kumar, S. Lahon, P. K. Jha, and M. Mohan, Superlattices Microstruct. **57**, 11 (2013).
[12] A. Abbout, G. Lemarié, and J. L. Pichard, Phys. Rev. Lett. **106**, 156810 (2011).
[13] E. J. Heller and S. Shaw, Int. J. Mod. Phys. B **17**, 3977 (2003).
[14] B. Liu and E. J. Heller, Phys. Rev. Lett. **111**, 236804 (2013).
[15] B. Liu, J. Phys.: Conf. Ser. **626**, 012037 (2015)
[16] K. Kolasiński, B. Szafran, and M. P. Nowak, Phys. Rev. B **90**, 165303 (2014).
[17] J. H. Davies, I. A. Larkin, and E. V. Sukhorukov, J. Appl. Phys. **77**, 4504 (1995).
[18] K. Kolasiński and B. Szafran, Phys. Rev. B **88**, 165306 (2013).
[19] B. Szafran, Phys. Rev. B **84**, 075336 (2011).
[20] R. Steinacher, A. A. Kozikov, C. Rössler, C. Reichl, W. Wegscheider, T. Ihn, and K. Ensslin, New J. Phys. **17**, 043043 (2015).
[21] M. Zwierzycki, P. A. Khomyakov, A. A. Starikov, K. Xia, M. Talanana, P. X. Xu, V. M. Karpan, I. Marushchenko, I. Turek, G. E. W. Bauer, G. Brocks, and P. J. Kelly, Phys. Status Solidi **245**, 623 (2008).
[22] T. Ando, Phys. Rev. B **44**, 8017 (1991).
[23] P. A. Khomyakov, G. Brocks, V. Karpan, M. Zwierzycki, and P. J. Kelly, Phys. Rev. B **72**, 035450 (2005).
[24] N. Paradiso, S. Heun, S. Roddaro, L. Pfeiffer, K. West, L. Sorba, G. Biasiol, and F. Beltram, Physica E **42**, 1038 (2010).
[25] A. A. Kozikov, C. Rössler, T. Ihn, K. Ensslin, C. Reichl, and W. Wegscheider, New J. Phys. **15**, 013056 (2013).
[26] R. Steinacher, A. A. Kozikov, C. Rössler, C. Reichl, W. Wegscheider, K. Ensslin, and T. Ihn, Phys. Rev. B **93**, 085303 (2016)
[27] B. Brun, F. Martins, S. Faniel, B. Hackens, A. Cavanna, C. Ulysse, A. Ouerghi, U. Gennser, D. Mailly, P. Simon, S. Huant, V. Bayot, M. Sanquer, and H. Sellier, Phys. Rev. Lett. **116**, 136801 (2016).
[28] C. S. Lent and D. J. Kirkner, J. Appl. Phys. **67**, 6353 (1990).
[29] K. Kolasiński, A. Mreńca-Kolasińska, and B. Szafran, Phys. Rev. B **93**, 035304 (2016)
[30] I. Rungger and S. Sanvito, Phys. Rev. B **78**, 035407 (2008).